

First-principles study of topological invariants of Weyl points in continuous media

Guilherme R. Fonseca ^{1,*}, Filipa R. Prudêncio ^{1,2}, Mário G. Silveirinha ¹ and Paloma A. Huidobro ^{1,3,†}

¹*Instituto de Telecomunicações, Instituto Superior Técnico-University of Lisbon, Avenida Rovisco Pais 1, Lisboa, 1049-001 Portugal*

²*Instituto Universitário de Lisboa (ISCTE-IUL), Avenida das Forças Armadas 376, 1600-077 Lisbon, Portugal*

³*Departamento de Física Teórica de la Materia Condensada and Condensed Matter Physics Center (IFIMAC), Universidad Autónoma de Madrid, E-28049 Madrid, Spain*



(Received 6 August 2023; revised 7 November 2023; accepted 13 November 2023; published 5 January 2024)

In recent years there has been a great interest in topological photonics and protected edge states. Here, we present a first-principles method to compute topological invariants of three-dimensional gapless phases. The approach enables the calculation of the topological charges of Weyl points through the use of the photonic Green's function of the system. We take two different approaches, and show that they are consistent. In the first one, we rely on the computation of Chern numbers in two-dimensional cross-sectional planes away from the Weyl point. The second approach is based on direct calculation of the Berry curvature around the Weyl point. We particularize the framework to the Weyl points that emerge in a magnetized plasma due to the breaking of time-reversal symmetry. We discuss the relevance of modeling nonlocality when considering the topological properties of continuous media such as the magnetized plasma. Our theory may be extended to other three-dimensional topological phases or to Floquet systems.

DOI: [10.1103/PhysRevResearch.6.013017](https://doi.org/10.1103/PhysRevResearch.6.013017)

I. INTRODUCTION

Topological states in photonics have attracted much attention due to the promise of light propagation protected from backscattering and thus immune to defects, such as sharp edges or corners of the medium surface [1–6]. Through the bulk-edge correspondence, a nontrivial topological invariant of the medium's bands guarantees protected edge modes that lie in the band gap, when the topological medium is interfaced with a trivial material, or vacuum [7,8]. The discovery of nontrivial topological phases in optics [1,2,9] was inspired by the electronic quantum Hall effect [10–12]. The topological invariants are integers designated by “Chern numbers.” Topological edge modes have been observed in photonic crystals [1,2,9] and in a number of other systems including waveguide arrays [13], and are also present in photonic continua [14–19].

Three-dimensional (3D) systems can also host gapless topological phases. This is the case of Weyl semimetals, characterized by point degeneracies between topologically inequivalent bands. These linear crossings between bands in 3D, named Weyl points, are robust against perturbations and are characterized by a quantized topological charge [6]. Weyl points have been realised in complex 3D photonic sys-

tems, such as photonic crystals [20,21] and metamaterials [22–24] as well as in homogeneous continuous media such as a magnetized plasma [25]. The associated protected surface states that emerge in the gaps away from the Weyl point [26] have been observed in photonic systems including photonic crystals [27,28], a strongly biased semiconductor [29] and a metamaterial [30].

Topological photonic systems are conventionally characterized by means of topological band theory [5,6,31,32]. This framework yields a band's Chern number from an integral of the Berry curvature in momentum space, which is in turn calculated from the system's eigenstates. This approach is usually taken for periodic photonic crystals, with momentum space integrals carried out in the Brillouin zone, and typically neglects dispersion, which is, however, an essential ingredient in topological continuous media, such as the magnetized plasma. An alternative approach to characterize Weyl points in the past has relied on linear $k \cdot p$ models around the Weyl point, which enables one to write a Hamiltonian for the system close to this degeneracy point [25].

In this work, we introduce a first-principles method to calculate topological invariants in 3D dispersive photonic systems, and we apply it to the study of the Weyl points in a magnetized plasma. In contrast to topological band theory, our approach is based on the Green's function and does not require the calculation of the system's eigenstates [33]. Additionally, dispersion is naturally included in the method, as well as nonlocality. In fact, it is known that a nonlocal material response must be taken into account to guarantee well-defined topologies in dispersive photonic systems [7,15,34–37]. Here, we find that nonlocality can also influence in a decisive way the type of Weyl points in an electromagnetic continuum. Additionally, nonlocality can also affect the number of Weyl

*guilhermefonseca@tecnico.ulisboa.pt

†p.arroyo-huidobro@uam.es

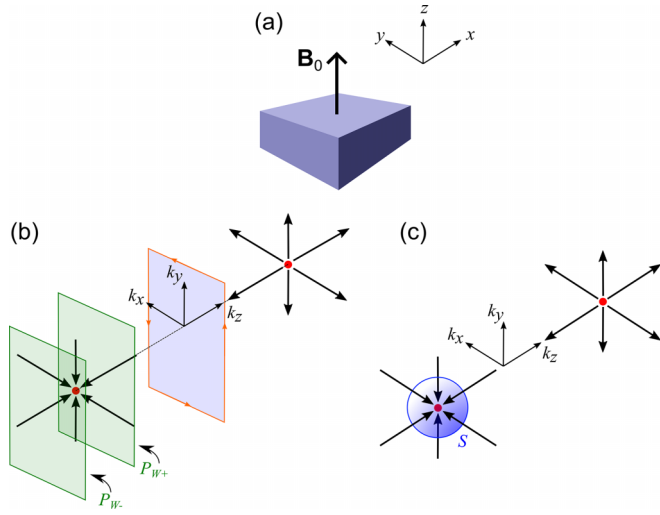


FIG. 1. Weyl points are monopoles of Berry curvature in momentum space. A plasma magnetized in the \hat{z} direction (a) hosts pairs of Weyl points aligned along the k_z axis. (b) A slice of momentum space between two Weyl nodes is a Chern insulator (blue plane) and hosts unidirectional edge states. The planes in green on the right (P_{W+}) and on the left (P_{W-}) of the Weyl point represent the cuts where the gap Chern numbers will be numerically computed and whose difference gives the topological charge of the Weyl point (Approach I). (c) The Weyl charge can be computed by integrating the flux of the Berry curvature through a spherical surface that surrounds the Weyl point (Approach II).

point pairs in this system. Different methods based on Green's functions and spectral localizers have been proposed by other authors [38–41]. Similar to our theory, these methods do not rely on the computation of the photonic spectrum.

The paper is organized as follows. First, in Sec. II we detail the methodology that allows us to compute the topological charges of Weyl points from first principles, based on two approaches: the first one is based on the calculation of the gap Chern numbers in two-dimensional (2D) cross-sectional planes away from the Weyl point under study; and the second one involves integrating the flux of the Berry curvature through an infinitesimal 3D momentum spherical surface centered at the Weyl point. Next, in Sec. III we present the results for the topological charge of Weyl points in a magnetized plasma. We first consider a local model which is known to yield noninteger topological invariants in 2D type systems [15]. To take into account the unavoidable nonlocality of the magnetized plasma, we then consider two models that incorporate a physical regularization procedure in the material response that ensures integer invariants: a nonlocal hydrodynamic model and a full spatial cutoff model. We discuss the Weyl points that emerge in both systems, as well as their differences.

II. ANALYTICAL FORMALISM

Weyl points are topological entities that originate from a geometric property of a system's eigenstates, the Berry curvature. Integration of the Berry curvature, $\mathcal{F}_n(\mathbf{k})$, over a closed spherical surface that encloses the point [see Fig. 1(c)] gives a

quantized quantity,

$$\int dS \hat{\mathbf{n}} \cdot \mathcal{F}_n(\mathbf{k}) = 2\pi C_W, \quad (1)$$

with $\hat{\mathbf{n}}$ a unit vector normal to the spherical integration surface in the outgoing direction and n an index that labels the bands. C_W , an integer, is the charge of the Weyl point. Its sign gives the chirality of the Weyl degeneracy, that is, determines if the flux is flowing into or away from the topological point. Thus, the amount of Berry flux that goes through any closed surface in momentum space that encloses the Weyl point is a topological invariant. This implies that Weyl points are monopoles of Berry curvature in 3D momentum space. They only exist in systems with a broken parity (\mathcal{P}) or time-reversal (\mathcal{T}) symmetries, or both, which explains their robustness against perturbations. In fact, they always appear in pairs, one being a source and the other a drain, linked by inversion symmetry, that can mutually annihilate [42]. Importantly, the sum of the chiralities of Weyl points in a system must vanish [32,43].

The Berry curvature in Eq. (1) can be written in terms of the Berry connection, $\mathcal{A}_n(\mathbf{k})$, as $\mathcal{F}_n(\mathbf{k}) = \nabla_{\mathbf{k}} \times \mathcal{A}_n(\mathbf{k})$, with $\mathcal{A}_n(\mathbf{k}) = \langle \Psi_n^\dagger(\mathbf{k}) | i \nabla_{\mathbf{k}} \Psi_n(\mathbf{k}) \rangle$, and $\Psi_n(\mathbf{k})$ the eigenstates. This in principle requires knowledge of the eigenfunctions along the 3D bands. Alternatively, it has been shown that the Berry curvature may be explicitly written in terms of the photonic Green's function, thus circumventing the need to compute the eigenstates along the full band structure [33,44]. The photonic Green's function is obtained from Maxwell's equations and can be written as

$$\mathcal{G}_{\mathbf{k}} = i(\hat{\mathcal{L}}_{\mathbf{k}} - \omega \mathbf{1})^{-1}, \quad (2)$$

where $\mathbf{1}$ is the identity and $\hat{\mathcal{L}}_{\mathbf{k}}$ is a frequency-independent differential operator that effectively models wave propagation in a dispersive medium. Typically, such a description entails modeling the effects of the material dispersion with additional variables that represent the internal degrees of freedom of the medium responsible for the dispersive response. The operator $\hat{\mathcal{L}}_{\mathbf{k}}$ is parameterized by the real wave vector \mathbf{k} and its eigenfrequencies coincide with the poles of $\mathcal{G}_{\mathbf{k}}$. The derivation of $\hat{\mathcal{L}}_{\mathbf{k}}$ for a magnetized plasma is presented in Appendix A.

For lossless media, the eigenfrequencies lie in the real frequency axis, separated by vertical strips that correspond to the band gaps. For bands separated by a band gap, the sum of the contributions of each of the Berry curvatures of the bands below the band gap $\mathcal{F}(\mathbf{k}) = \sum_n \mathcal{F}_n(\mathbf{k})$ is then obtained through an integral in the complex frequency space over a line parallel to the imaginary axis contained in the band gap ($\omega = \omega_{\text{gap}} + i\infty$). The l component ($l = x, y, z$) of the Berry curvature can be written as [44–46]

$$[\mathcal{F}(\mathbf{k})]_l = \frac{\epsilon_{lmn}}{2} \frac{i}{2\pi} \int_{\omega_{\text{gap}} - i\infty}^{\omega_{\text{gap}} + i\infty} d\omega \text{Tr} \{ \partial_m \hat{\mathcal{L}}_{\mathbf{k}} \cdot \mathcal{G}_{\mathbf{k}} \cdot \partial_n \hat{\mathcal{L}}_{\mathbf{k}} \cdot \mathcal{G}_{\mathbf{k}}^2 \}, \quad (3)$$

where we have generalized the expression for 2D Chern insulators [44–46] to 3D media. The summation over $m, n = 1, 2, 3$ is implicit. Note that interchanging m and n flips the sign of the integral. Here, ϵ_{lmn} is the Levi-Civita symbol, Tr is the trace operator, $\partial_i = \partial/\partial k_i$ ($i = x, y, z$) and ω_{gap} is some frequency contained within the band gap. This approach is

valid for dispersive continuous media, as well as for photonic crystals [37].

We next show that the topological invariant of the Weyl points can be calculated from the Green's function, through two complementary approaches. We assume a system with broken \mathcal{T} , where a minimum of two Weyl points appear at opposite momenta, as sketched in Fig. 1. The same procedure can be applied to systems with broken \mathcal{P} which host a minimum of two pairs of Weyl points.

A. Approach I: Chern number difference

Consider the topological charge of one of the two Weyl points of a pair, C_W in Eq. (1). The surface integral in that equation can be carried out in an infinitesimally small sphere enclosing the Weyl point. By construction, inside the integration volume the bands are well separated by a band gap and the Berry curvature is well defined for the bands of interest everywhere except at the Weyl point. Thus, the divergence of the Berry curvature is zero everywhere except at the singularity, and through Stokes theorem the integration surface can be deformed into a parallelepiped. Therefore, the integral can be equivalently carried out on the surface of a rectangular slice of momentum space perpendicular to the axis along which the Weyl point pairs are aligned [the k_z axis in the sketch of Fig. 1(b)]. Then, the topological invariant amounts to a sum of the Berry fluxes going through all the sides of this parallelepiped. Furthermore, the choice of integration surface ensures that there are no other sources of Berry flux enclosed by it, such that we can take the side faces (parallel to the k_z axis) to infinity where their contribution vanishes, and obtain the topological invariant from the Berry fluxes going through the two planes orthogonal to the k_z axis at either side of the Weyl point, P_{W-} and P_{W+} , sketched in green in Fig. 1(b). Thus, the expression for the topological charge, Eq. (1), transforms into

$$C_W = \frac{1}{2\pi} \int_{P_{W-}} d^2\mathbf{k} (-\hat{\mathbf{z}}) \cdot \mathcal{F}_n(\mathbf{k}) + \frac{1}{2\pi} \int_{P_{W+}} d^2\mathbf{k} \hat{\mathbf{z}} \cdot \mathcal{F}_n(\mathbf{k}), \quad (4)$$

where the relative sign between the two terms takes into account that the unit vector $\hat{\mathbf{n}}$ in Eq. (1) points outwards from the parallelepiped's surface. Here, $\hat{\mathbf{z}}$ is the unit vector along k_z . Additionally, the label n corresponds to the band that lies below the Weyl point.

The integrals in Eq. (4) correspond to the Chern numbers of a given band at each side of the Weyl point, in particular, the band that lies below it. Furthermore, since the bands only touch at the Weyl point and there are well defined band gaps at each side of it, the Chern numbers of the bands can be replaced by gap Chern numbers, defined as the sum of the individual Chern numbers of the bands immediately below a band gap $C_{\text{gap}} = \sum_n C_n$. Hence,

$$C_W = C_{\text{gap}}(P_{W+}) - C_{\text{gap}}(P_{W-}). \quad (5)$$

From topological band theory, the gap Chern number can be calculated from the Berry curvature:

$$c_{\text{gap}} = \frac{1}{2\pi} \iint d^2\mathbf{k} \hat{\mathbf{z}} \cdot \mathcal{F}(\mathbf{k}). \quad (6)$$

The gap Chern number of each spectral band gap can also be calculated from first principles using the photonic Green's function of the medium, as was shown in Refs. [33,37,45,47]. Specifically,

$$C_{\text{gap}} = \frac{i}{(2\pi)^2} \iint d^2\mathbf{k} \int_{\omega_{\text{gap}}-i\infty}^{\omega_{\text{gap}}+i\infty} d\omega \text{Tr}\{\partial_1 \hat{L}_{\mathbf{k}} \cdot \mathcal{G}_{\mathbf{k}} \cdot \partial_2 \hat{L}_{\mathbf{k}} \cdot \mathcal{G}_{\mathbf{k}}^2\}, \quad (7)$$

where the integral over \mathbf{k} is carried out over the whole momentum space.

Hence, with this approach the topological charge of a Weyl point is obtained by computing the gap Chern number of the frequency band gaps that exist at each side of the Weyl point in momentum space. Pairs of Weyl points bound planes of Chern insulators with nontrivial gap Chern numbers, while outside of the pairs the system will be trivial [42].

B. Approach II: Direct integration of the Berry curvature

An alternative approach to compute Weyl charges can be accomplished through direct integration of the Berry curvature. In particular, from the expression of the Berry curvature in terms of the Green's function, Eq. (3), we can write explicitly,

$$\begin{aligned} \mathcal{F}(\mathbf{k}) \cdot \hat{\mathbf{n}} = & \frac{i}{2\pi} \int_{\omega_{\text{gap}}-i\infty}^{\omega_{\text{gap}}+i\infty} d\omega \text{Tr}\{[n_1 \partial_2 \hat{L}_{\mathbf{k}} \cdot \mathcal{G}_{\mathbf{k}} \cdot \partial_3 \hat{L}_{\mathbf{k}} \\ & + n_2 \partial_3 \hat{L}_{\mathbf{k}} \cdot \mathcal{G}_{\mathbf{k}} \cdot \partial_1 \hat{L}_{\mathbf{k}} + n_3 \partial_1 \hat{L}_{\mathbf{k}} \cdot \mathcal{G}_{\mathbf{k}} \cdot \partial_2 \hat{L}_{\mathbf{k}}] \cdot \mathcal{G}_{\mathbf{k}}^2\}. \end{aligned} \quad (8)$$

From Eq. (1) we see that the topological charge of the Weyl point can be obtained by direct integration of the above quantity over a spherical surface in 3D momentum space enclosing the Weyl point.

Due to the geometry of the integration surface, it is convenient to adopt a system of spherical coordinates to parametrize the wave vector space. We describe the 3D momentum sphere around the Weyl point with polar angle θ , azimuthal angle ϕ and k its radius. The wave vector can thus be written as $\mathbf{k} = \mathbf{k}_W + k\hat{\mathbf{n}}$, where \mathbf{k}_W is the momentum location of the Weyl point and the unit vector normal to the sphere is parametrized as $\hat{\mathbf{n}} = (\cos\phi \sin\theta, \sin\phi \sin\theta, \cos\theta)$. This approach allows us to directly compute the topological charge of the Weyl points from the Green's function of the system. A subtlety arises since it is not obvious that the modes in the parametrized momentum space are fully gapped so the frequency integral in Eq. (8) has to be done carefully. This is further discussed in Sec. III D.

In the following section we apply our framework to study a continuous medium with nontrivial topology featuring Weyl points: a magnetized plasma [25]. The direct integration of the Berry curvature (Sec. II B) will serve as the baseline against which we will compare the results obtained from approach I (Sec. II A), which solely relies on computing gap Chern numbers over a slice of the "Brillouin zone" (an unbounded plane for a continuum). We consider three different models of the magnetized plasma, a local and two nonlocal models, and

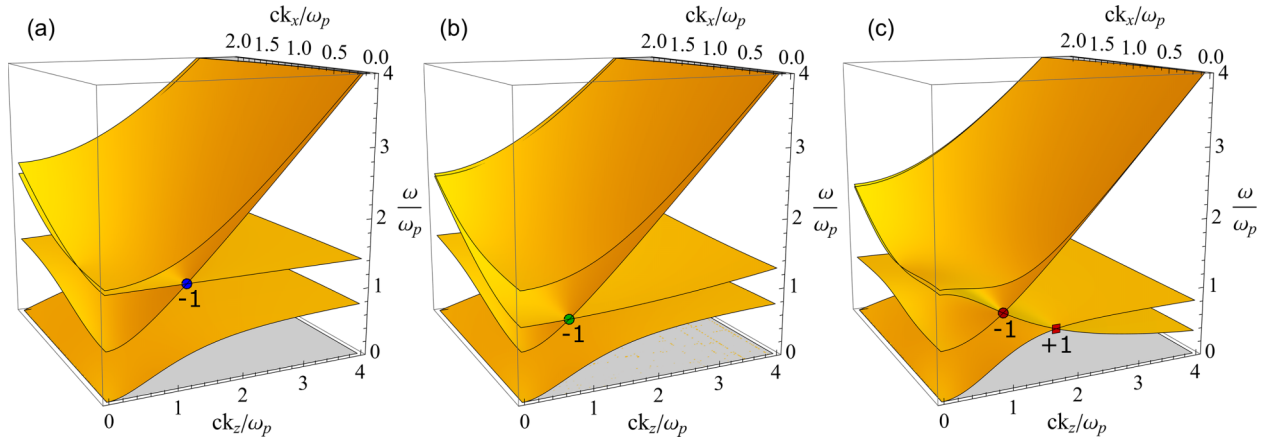


FIG. 2. Three-dimensional dispersion of local and nonlocal magnetized plasma models. (a) Dispersion surfaces for the local Drude model described in Sec. III A, with parameters $\omega_c = 0.8\omega_p$ and $\omega'_p = \sqrt{2}\omega_p$. (b) Dispersion surfaces for a magnetized plasma described by a hydrodynamic model with $\beta = 0.2c$ and $\omega_c = 0.8\omega_p$. (c) Dispersion surfaces for a magnetized plasma described with a full spatial cutoff model with $k_{\max} = \omega_p/c$, $\omega_c = 0.8\omega_p$, and $\omega'_p = \sqrt{2}\omega_p$. The integer numbers represent the topological charge of each Weyl point and they were computed with Approach II [Eqs. (1) and (8)].

show that including nonlocality is important in the study of topological properties of homogeneous photonic Weyl media.

III. TOPOLOGICAL CHARACTERIZATION OF MAGNETIZED PLASMA

Let us consider a 3D plasma biased with a magnetic field applied along the $\hat{\mathbf{z}}$ direction, as sketched in Fig. 1(a). The medium is characterized by a plasma frequency ω_p and a cyclotron frequency ω_c . Throughout this work, we consider lossless local and nonlocal models of magnetized plasma, with a nonmagnetic response, $\bar{\mu} = \mu_0 \mathbf{1}$. We start with the simpler, local model, in Sec. III A. Next, since we deal with an unbounded wave vector space, we introduce nonlocality to take into account that there is a physical cutoff that suppresses the material response for large wave vectors (i.e., for very fast variations of the field in space). Nonlocality results in a wave vector-dependent permittivity. The nonlocal hydrodynamic model in Sec. III B takes this into account by incorporating charge diffusion due to repulsions between the electrons in the plasma. A different approach is the nonlocal full-cutoff model of Sec. III C. It was shown in Refs. [15,17,18], that the full cutoff effectively models the fact that the material is formed by discrete elements (atoms) standing in a vacuum (empty space), and that this granularity results in a short-wavelength cutoff. It should be noted that the type of nonlocality in the plasma depends on the processes that control the electrodynamics on a microscopic scale. Thus, the correct cutoff may not be universal as it depends on the microscopic features of the material. The nonreciprocal edge modes supported by a magnetized plasma in the plane transverse to the magnetic field are already well studied, taking the 3D medium as translationally invariant and reducing it to a 2D problem [7,15,34–37,48].

Breaking of \mathcal{T} -symmetry enables the emergence of Weyl point pairs in this 3D system [25]. The Weyl points arise as linear crossings between longitudinal and transverse modes along the k_z axis, as imposed by the direction of the applied magnetic field. As \mathcal{P} -symmetry is preserved, $\omega(-\mathbf{k}) = \omega(\mathbf{k})$,

and each Weyl crossing with positive momentum k_z has a partner at a symmetric point $-k_z$. The 3D dispersion surfaces of magnetized plasmas with different nonlocal properties can be seen in Fig. 2: a local model is considered in Fig. 2(a), and two different nonlocal models in Figs. 2(b) and 2(c), which will be described below. Weyl crossings at positive k_z can be seen in all cases, marked with a blue, green, or red dot in each panel. As mentioned, \mathcal{P} -symmetry ensures that band structures are symmetric between \mathbf{k} and $-\mathbf{k}$, so we only show positive k_z . Next to each Weyl point, we show the topological charge which was computed by integrating the Berry curvature flux over a small spherical surface centered at the Weyl point [through Eqs. (1) and (8)]. Details on this approach are given in the last part of Sec. III D.

The Weyl points predicted by the local model are predicted as well by the nonlocal models. The corresponding topological charges are independent of the model. This property is in contrast with the gap Chern numbers of the associated 2D systems, which depend critically on the nonlocality [7,15,34–37]. Crucially, gap Chern numbers are ill-defined if the medium response is not properly regularized. In contrast, Weyl charges depend on the medium response near the finite Weyl momentum and are always well defined and consistent between different models, although new Weyl pairs can appear in some of the models, as we will see below. However, the type of Weyl point exhibited by the system is affected by the nonlocality.

A. Local model

We first discuss the local magnetized plasma. The permittivity tensor that describes electromagnetic propagation in the bulk of this continuum is a matrix with a gyrotropic structure [49,50]:

$$\frac{\bar{\epsilon}(\omega)}{\epsilon_0} = \mathbf{1} + \frac{\omega_p^2}{\omega} \left[-\omega \mathbf{1} + i\omega_c \hat{\mathbf{z}} \times \mathbf{1}_t \right]^{-1} = \begin{bmatrix} \epsilon_t & -i\epsilon_g & 0 \\ i\epsilon_g & \epsilon_t & 0 \\ 0 & 0 & \epsilon_z \end{bmatrix}, \quad (9)$$

where $\mathbf{1}_t = \hat{\mathbf{x}} \otimes \hat{\mathbf{x}} + \hat{\mathbf{y}} \otimes \hat{\mathbf{y}}$, and with \times as the cross product and \otimes as the tensor product. Each matrix component is

$$\epsilon_t = 1 - \frac{\omega_p^2}{\omega^2 - \omega_c^2}, \quad \epsilon_g = \frac{-\omega_c \omega_p^2}{\omega(\omega^2 - \omega_c^2)}, \quad \epsilon_z = 1 - \frac{\omega_p^2}{\omega^2}. \quad (10)$$

The lack of transpose symmetry is a consequence of breaking time-reversal symmetry (\mathcal{T}) through the application of the magnetic field, turning the plasma into a nonreciprocal medium. It has been shown that this medium possesses one pair of Weyl points when $\omega_c < \omega_p$, and two pairs when $\omega_c > \omega_p$, an inner and outer Weyl pair [25].

The local model considered in this work has a permittivity tensor $\bar{\epsilon}_{\text{loc}}$ which is the same as in Eq. (9), but with a uniaxial plasma response, characterized with a different plasma frequency in the $\hat{\mathbf{z}}$ direction, ω'_p . Only the $\hat{\mathbf{z}} \otimes \hat{\mathbf{z}}$ component is affected by this choice: $\epsilon_z = \epsilon_0(1 - \omega_p'^2/\omega^2)$. Under these conditions, this model only possesses one Weyl pair and full band gaps are ensured in the xoy plane away from the Weyl points. The Weyl points location is given by

$$k_z = \pm k_z^W = \pm \sqrt{\frac{\omega'_p(\omega_p'^2 + \omega_c \omega'_p - \omega_p^2)}{c^2(\omega_c + \omega'_p)}}. \quad (11)$$

The Weyl points arise along the direction of the magnetic field in momentum space, k_z , as a linear crossing between a flat longitudinal plasmon mode with constant frequency $\omega = \omega'_p$ and a transverse mode. The Weyl point with positive k_z is highlighted with a blue dot in Fig. 3(a), and as previously mentioned the bands are symmetric under $k_z \rightarrow -k_z$ (not shown here). As they stem from the flat longitudinal mode, the pointlike degeneracies displayed by this model are tilted Weyl points that exhibit parabolic isofrequency surfaces around them [25]. They stand at the critical transition between type-I Weyl points, with ellipsoidal isofrequency surfaces, and type-II Weyl points, for which the isofrequency surface is a hyperboloid [22].

The Weyl charge can be obtained as the difference of gap Chern numbers. To do this, we consider the dispersion in cross-sectional planes of the 3D bands orthogonal to the k_z axis. The gap Chern numbers are calculated for the planes at the left and right-hand sides of the Weyl point. Figure 3(b) depicts a cross section of the 3D dispersion at $k_z = 0$ (xoy plane), which displays two band gaps: a low-frequency one, bounded between zero-frequency mode and a low-frequency transverse magnetic (TM) band (shaded in orange); and a high-frequency gap between the same TM mode and a transverse electric (TE) mode (shaded in blue). The Chern numbers of these band gaps have been previously studied [15,33,51], and analytical expressions have been found (for $k_z = 0$). The gap Chern numbers take into account the topological charge of negative frequency bands (not shown in Fig. 3), as they are given by the sum of the Chern numbers of all bands below it. For the high-frequency band gap (highlighted in blue), $C_{\text{gap},1} = +1$, while for the low-frequency one $C_{\text{gap},2} = -1/\sqrt{1 + \omega_p^2/\omega_c^2}$. The latter result, a noninteger gap Chern number, is a consequence of the ill-defined topology of the low-frequency TM mode due to the limitations of the local model.

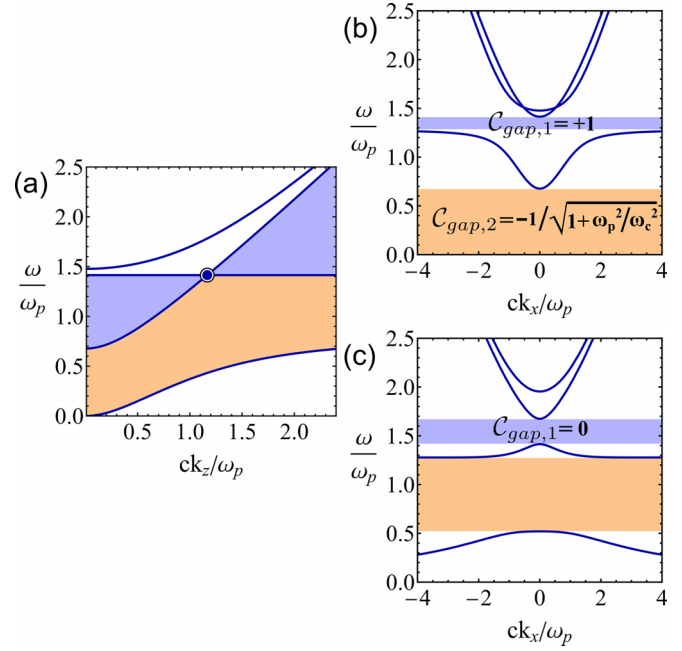


FIG. 3. Frequency dispersion for a local magnetized plasma, in cross sections of Fig. 2(a). (a) Dispersion along the k_z axis exhibiting one of the Weyl points of the pair marked with a blue circle. The band gaps of interest are shaded in blue and orange. (b), (c) Dispersion in cross-sectional planes orthogonal to the k_z axis, before and after the Weyl point: $k_z = 0$ (b) and $k_z = \frac{5}{4}k_z^W$ (c). The parameters used here were $\omega_c = 0.8\omega_p$ and $\omega'_p = \sqrt{2}\omega_p$.

Next we take a cross section of the dispersion at the right-hand side of the Weyl point, in particular at $k_z = \frac{5}{4}k_z^W$ [see Fig. 3(c)]. As k_z increases from $k_z = 0$, the low-frequency TM mode bends upwards and crosses the flat TE mode at the Weyl point. This band crossing enables an exchange of topological charge, and thus modifies the gap Chern number of the high-frequency (blue) band gap. We confirm this numerically [Eq. (7)] by computing the gap Chern number, which yields $C_{\text{gap},1} = 0$. However, the low-frequency (orange) band gap does not close and thus its topological invariant stays a noninteger number, decreasing as k_z increases. Additionally, the results are symmetric for negative momentum values ($k_z = -k_z^W$), due to the spatial parity symmetry of the Berry curvature $\mathcal{F}(-\mathbf{k}) = \mathcal{F}(\mathbf{k})$ [25,52]. Thus, we have that for $k_z \in (-\infty, -k_z^W)$, $C_{\text{gap},1} = 0$, while for $k_z \in (-k_z^W, k_z^W)$, $C_{\text{gap},1} = +1$ and for $k_z \in (k_z^W, \infty)$, $C_{\text{gap},1} = 0$. From this we compute the topological charge of the Weyl pair following Eq. (4) as $C_W(k_z = -k_z^W) = (+1) - 0 = +1$ for the one at negative momentum, and $C_W(k_z = +k_z^W) = 0 - (+1) = -1$ for the one at positive momentum. The calculation agrees with the result discussed earlier obtained by direct integration of the Berry curvature flux through the spherical surface centered at the Weyl point. This is also consistent with the results obtained in Ref. [25] for a local magnetized plasma using a $\mathbf{k} \cdot \mathbf{p}$ expansion close to the Weyl points. As expected, having $\omega'_p \neq \omega_p$ in the permittivity tensor does not change the topological properties of the magnetized plasma, which shows one pair of Weyl points with charge ± 1 for $\omega_c < \omega_p$. Due to the continuous and local nature of this medium, some of its

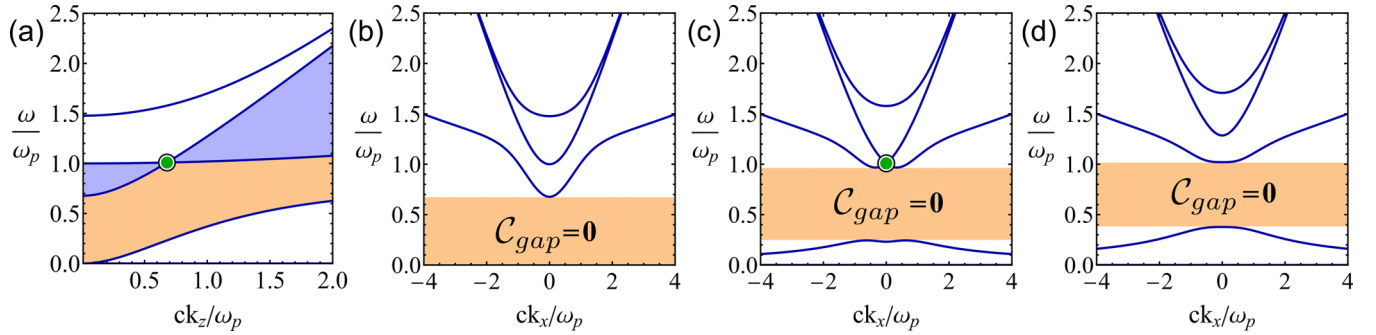


FIG. 4. Frequency dispersion for the hydrodynamic model: (a) in the k_z axis exhibiting the two regions of interest shaded in blue and orange. [(b)–(d)] Cross sections of the 3D dispersion [Fig. 2(b)] for different values of k_z : (b) $k_z = 0$, (c) $k_z = k_z^W$, and (d) $k_z = \frac{3}{2}k_z^W$. The band gaps are highlighted in orange. The Weyl crossing is highlighted with the green circle. The parameters used here were $\beta = 0.2c$ and $\omega_c = 0.8\omega_p$.

topological features are ill-defined when the integration surface in momentum space is unbounded. To overcome this problem, some cutoff should be included to the material response, to ensure that its nonreciprocal components are suppressed for large wave vectors [15]. When dealing with realistic materials, fields with very fast spatial variation cannot effectively polarize the microscopic constituents of the medium, therefore its response is effectively suppressed when $k \rightarrow \infty$ and it should reduce to that of the vacuum, so the momentum cutoff has a physical justification [53]. For this purpose, we next consider two different nonlocal models: the hydrodynamic model and the full-cutoff model.

B. Hydrodynamic model

A conventional approach to consider nonlocal effects is to employ the hydrodynamic model, where the repulsive interactions between electrons are accounted for by adding a diffusion-type force contribution to the transport equation [54]. The diffusion velocity, β , is introduced as a parameter. It controls the diffusion strength and typically corresponds to the velocity of electrons at the Fermi level. The permittivity tensor within this model can be written as

$$\frac{\bar{\epsilon}_{\text{hydro}}}{\epsilon_0}(\omega, \mathbf{k}) = \mathbf{1} + \frac{\omega_p^2}{\omega} \left[-\omega \mathbf{1} + i\omega_c \hat{\mathbf{z}} \times \mathbf{1}_t + \frac{\beta^2}{\omega} \mathbf{k} \otimes \mathbf{k} \right]^{-1}, \quad (12)$$

where we observe how the last term on the right hand side introduces an explicit dependence on the momentum.

Dispersion surfaces for this model are shown in Fig. 2(b), for a choice of parameters given in the figure caption with one pair of Weyl points, at $k_z = \pm k_z^W$, marked with a green dot in the figure. Cross sections of the dispersion, along the k_z axis and at three transverse cuts are shown in Fig. 4. Only the longitudinal modes are affected by nonlocality [15]. This can be observed in the dispersion of modes along k_z [Fig. 4(a)], where the flat longitudinal mode of the local model gains a positive group velocity ($\frac{\partial\omega}{\partial k} > 0$, for positive k), and also in the in-plane dispersion [Figs. 4(b)–4(d), for different values of k_z], where the low-frequency TM mode now bends upward. This is an important detail because the high-frequency band gap is consequently eliminated in every cross section, for any k_z value, in contrast to the results obtained with the local

model [see Fig. 3(b)]. The introduction of arbitrarily weak nonlocality of this type creates a type-II Weyl system, as can be attested by the hyperbolic isofrequency curves around the linear crossing seen in Fig. 5. This is the case when the crossing between the longitudinal mode and the transverse mode have group velocities $v_g = \frac{\partial\omega}{\partial k}$ with the same sign. This type of Weyl point has a diverging local density of states (DOS) at the Weyl frequency [24].

Due to the closing of the high-frequency band gap in planes transverse to the k_z axis within this model, Approach I can only be applied to the low-frequency band gap, highlighted in orange in Fig. 4. Direct computation of the gap Chern number for this band gap yields $C_{\text{gap}} = 0$, at any cross-sectional plane, as seen for a plane in between the two Weyl points, $k_z = 0$, in Fig. 4(b), a plane at the Weyl point, $k_z = k_z^W$, in Fig. 4(c), and after the Weyl point, $k_z = \frac{3}{2}k_z^W$, in Fig. 4(d). This is consistent with the fact that this band gap never closes, either with a Weyl crossing or any other type of degeneracy [see Fig. 2(b)], such that the topological invariant of the gap cannot change.

With the hydrodynamic model, we cannot then obtain information on the topological charge of the Weyl point, as a

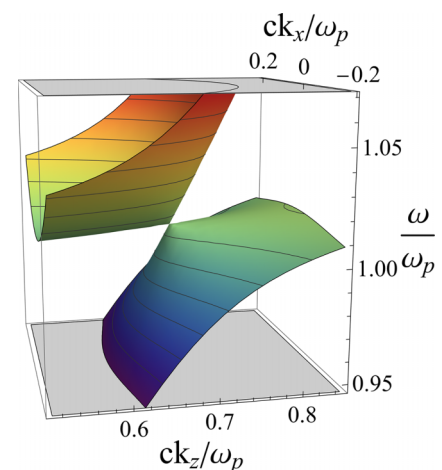


FIG. 5. The hydrodynamic model features type-II Weyl points: dispersion surfaces and isofrequency curves around the Weyl point at $k_z = +k_z^W$ in the $\hat{\mathbf{z}}$ and $\hat{\mathbf{x}}$ directions. The parameters used here were $\beta = 0.2c$ and $\omega_c = 0.8\omega_p$.

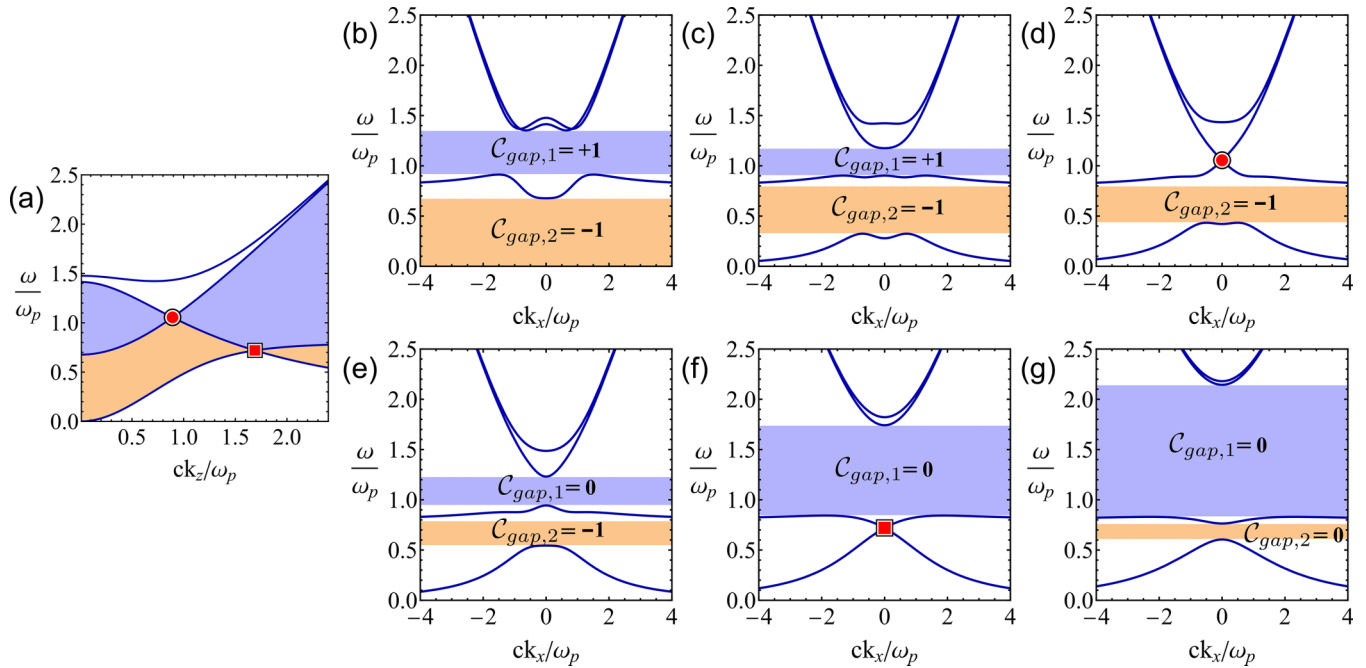


FIG. 6. Frequency dispersion for the full-cutoff model: (a) in the k_z axis exhibiting the two regions of interest in blue and orange. [(b)–(g)] Cross sections of the 3D dispersion [Fig. 2(c)] for different k_z values: (b) $k_z = 0$, (c) $k_z = \frac{3}{4}k_z^{W,1}$, (d) $k_z^{W,1}$, (e) $k_z = \frac{5}{4}k_z^{W,1}$, (f) $k_z^{W,2}$, and (g) $k_z = \frac{5}{4}k_z^{W,2}$. In panels [(b)–(g)], the high-frequency band gaps are highlighted in blue, the low-frequency ones in orange. The inner Weyl point at $k_z^{W,1}$ is highlighted with the red circle and the outer Weyl point with the red square at $k_z^{W,2}$. The parameters used here were $k_{\max} = \omega_p/c$, $\omega_c = 0.8\omega_p$, and $\omega'_p = \sqrt{2}\omega_p$.

gap Chern number difference, as it results from a crossing between high-frequency bands (see Fig. 4) and the lack of full frequency band gap along transverse directions prevents the application of the Green's function method. By direct integration we find $C_W = \pm 1$. We next consider a different and more general nonlocal model.

C. Full-cutoff Model

A general solution to regularize the topology of a continuum was introduced in Ref. [15], based on the introduction of a high-frequency spatial cutoff to the material response of a system, as

$$\bar{\epsilon}_{\text{cutoff}}(\omega, \mathbf{k}) = \epsilon_0 \mathbf{1} + \frac{1}{1 + k^2/k_{\max}^2} [\bar{\epsilon}_{\text{loc}}(\omega) - \epsilon_0 \mathbf{1}], \quad (13)$$

where $\bar{\epsilon}_{\text{loc}}$ stands for the original local response, $k^2 = \mathbf{k} \cdot \mathbf{k}$ and k_{\max} models the high-frequency wave vector cutoff. For large values of the wave vector, $k \gg k_{\max}$, the material response is suppressed, since for $k \rightarrow \infty$, $\bar{\epsilon}_{\text{cutoff}}(\omega, \mathbf{k}) \rightarrow \epsilon_0 \mathbf{1}$ and the material response becomes that of free space.

Unlike the hydrodynamic model, the nonlocality induced by this regularization affects all of the dispersion modes, albeit in a different way than the hydrodynamic model. Most importantly, the longitudinal mode along the k_z axis again acquires a nonzero group velocity, but this time a negative one ($\frac{\partial \omega}{\partial k} < 0$, for positive k), as can be observed in Fig. 6(a). Additionally, the frequency of the longitudinal mode now tends to zero $\omega \rightarrow 0$ as $k \rightarrow \infty$ and consequently this mode always intersects the other two transverse modes. This originates two pairs of Weyl points whose momentum space locations

will be designated as $k_z = \pm k_z^{W,1}$ for the inner crossing, and $k_z = \pm k_z^{W,2}$ for the outer crossing. The appearance of the outer Weyl point pair is a difference with respect to the local and hydrodynamic models. As it should, as the cutoff approaches infinity this pair migrates to infinity and the result of the local model is recovered. However, we note that the local model studied elsewhere [25] (without uniaxial response ω'_p in $\hat{\mathbf{z}}$) can present two pairs when $\omega_c > \omega_p$, that is, for a different set of parameters as those considered in our work. The physics of these Weyl crossings is distinct from that of those appearing in the hydrodynamic model, due to the different signs of the group velocities of each crossing mode. In this case, the isofrequency curves around all Weyl points are closed ellipses, with a vanishing DOS exactly at the Weyl frequency, making this a type-I Weyl system. This is shown in Fig. 7 for the inner Weyl point, $k_z = +k_z^{W,1}$. This confirms that nonlocality has a crucial role in determining the type and number of Weyl points exhibited in a system [22].

We now consider the band structures in planes transverse to the k_z axis, see Figs. 6(b)–6(g), to compute the topological charge of the Weyl points hosted by the system. As in the previous sections, we consider dispersion curves $\omega(k_x)$, for different values of k_z . As with the hydrodynamic model, we start at $k_z = 0$ (b), where this time we identify two band gaps: a high-frequency one, highlighted in blue, and a low-frequency one, highlighted in orange. Computation of the gap Chern numbers yields $C_{\text{gap},1} = +1$ (blue band gap) and $C_{\text{gap},2} = -1$ (orange band gap). In contrast to the local magnetized plasma, the Chern numbers are now well defined due to the regularization provided by the spatial cutoff, and in

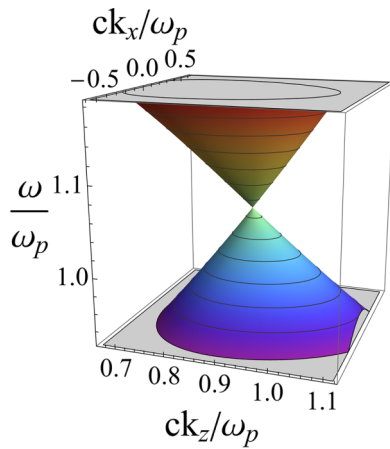


FIG. 7. The full spatial cutoff model features type-I Weyl points: dispersion surfaces and isofrequency curves around the inner Weyl point at $k_z = k_z^{W,1}$ in the \hat{z} and \hat{x} directions. The parameters used here were $k_{\max} = \omega_p/c$, $\omega_c = 0.8\omega_p$, and $\omega'_p = \sqrt{2}\omega_p$.

contrast to the hydrodynamic model, we observe two nontrivial band gaps. These results are consistent with those obtained in Ref. [15], where the magnetized plasma modes at $k_z = 0$ were studied. Next, Fig. 6(c) shows the band dispersion away from $k_z = 0$ but still at the left of the first Weyl point, $k_z = \frac{3}{4}k_z^{W,1}$. In this transverse plane, the zero-frequency mode is lifted, but the two band gaps are still preserved, as expected. Numerical computation confirms that the Chern numbers are still $C_{\text{gap},1} = +1$ and $C_{\text{gap},2} = -1$, as expected since the gaps have not closed. At the first Weyl point, $k_z = k_z^{W,1}$, the high-frequency band gap closes at this linear degeneracy, as shown in panel (d), while the low-frequency one is maintained, with $C_{\text{gap},2} = -1$, as expected too. Further increasing the value of k_z to $k_z = \frac{5}{4}k_z^{W,1}$, in between the two Weyl points, we see in Fig. 6(e) how the high-frequency gap opens up again, although the calculated gap Chern number is now $C_{\text{gap},1} = 0$. At the same time, the lower frequency band gap does not close in this process and hence $C_{\text{gap},2} = -1$ is kept. This band gap only closes in Fig. 6(f), at the second Weyl point, $k_z = k_z^{W,2}$. Finally, for k_z at the right of this outer degeneracy, we find this band gap is open again [Fig. 6(g)], and its gap Chern number turns trivial, $C_{\text{gap},2} = 0$, such that all band gaps are now trivial. This is expected as this should be the behavior at $k \rightarrow \infty$, and there are no more band gap closings after the outer Weyl point that could enable a change in topological invariants.

Once we know all the gap Chern numbers, we can calculate the magnitude of the topological charge of the Weyl point using Approach I [Eq. (5)]. We obtain, for the inner Weyl point at positive momentum, $C_W(k_z = +k_z^{W,1}) = 0 - (+1) = -1$, while its counterpart at negative momentum has charge $C_W(k_z = -k_z^{W,1}) = +1 - 0 = +1$. This value of the topological charge is consistent with the one obtained in the local model, as should be expected. Additionally, the topological charges of the outer Weyl pair are $C_W(k_z = +k_z^{W,2}) = 0 - (-1) = +1$ for the Weyl crossing with positive momentum and $C_W(k_z = -k_z^{W,2}) = (-1) - 0 = -1$ for the crossing with negative momentum. The outer pair of Weyl points smoothly

moves to infinity by increasing k_{\max} , thus retrieving the results from the local model.

D. Topological characterization with Approach II

In this section we give some details on how to directly compute the topological charge of Weyl points in the magnetized plasma. Particularly, we focus on the complex frequency integral of Eq. (8) and how the integral path can be implemented in the case of a 3D spherical momentum space.

We begin by plotting the frequency dispersion of the modes present in a 3D momentum sphere surrounding a Weyl point, for the three studied models. These modes are plotted in yellow in Fig. 8, parametrized by the spherical coordinates θ and ϕ (see Fig. 10 and Appendix B for more details). We see that only the full-cutoff model in Fig. 8(c) possesses a complete photonic band gap in the momentum sphere. And so, it is possible to compute the frequency integral in Eq. (8) along a path with a constant ω_{gap} , represented by the constant frequency plane in blue, between the two modes that intersect at the Weyl point. This is not feasible in the case of the local model in Fig. 8(a) and in the hydrodynamic model in Fig. 8(b), since there is no complete band gap. Nonetheless, it is possible to adjust $\omega_{\text{gap}}(\mathbf{k})$ along the wave vector space, and specifically for this case, for any (θ, ϕ) point. This procedure is justified because the Berry curvature in Eq. (3) is independent of the integration path in the gap. In the case of both these models, we parametrized the real part of the integral path $\omega_{\text{gap}}(\theta, \phi)$ with a smooth continuous function: $\omega_{\text{gap}} = \omega_{\text{Weyl}}(1 + A \cos \theta)$, where ω_{Weyl} is the frequency of the respective Weyl point and A is a suitable constant. We can observe these parametrizations represented by the blue surfaces in Figs. 8(a) and 8(b) of the same figure.

This approach allows to effectively calculate the Berry curvature of the bands that lie below the Weyl point for each wave vector value on the momentum sphere. The topological charge of the Weyl point is indeed well-defined because the low-frequency mode never intersects the high-frequency one, in the spherical surface, and so the integral yields an integer value. The topological charges obtained through this approach are given in Fig. 9. For the case of the local model, the calculation yields a charge of -1 for the positive momentum Weyl point ($k_z = +k_z^W$) and the negative counterpart possesses a charge of $+1$ ($k_z = -k_z^W$). We obtained identical results for the case of the hydrodynamic model, where the positive momentum Weyl point exhibits a topological charge of -1 ($k_z = +k_z^W$) and opposite charge of $+1$ for the negative counterpart ($k_z = -k_z^W$). This confirms the topological charge of the Weyl point shared by the local and hydrodynamic models is not influenced by the nonlocal properties of the medium, which control mainly the short wavelength physics ($k \rightarrow \infty$). Finally, the results for the full-cutoff model are consistent for the inner Weyl point pair, where the positive momentum inner Weyl point has charge -1 ($k_z = +k_z^{W,1}$) and $+1$ for the counterpart ($k_z = -k_z^{W,1}$). The outer Weyl points have switched signs relatively to the inner ones, where the positive momentum one possesses $+1$ ($k_z = +k_z^{W,2}$) and the negative

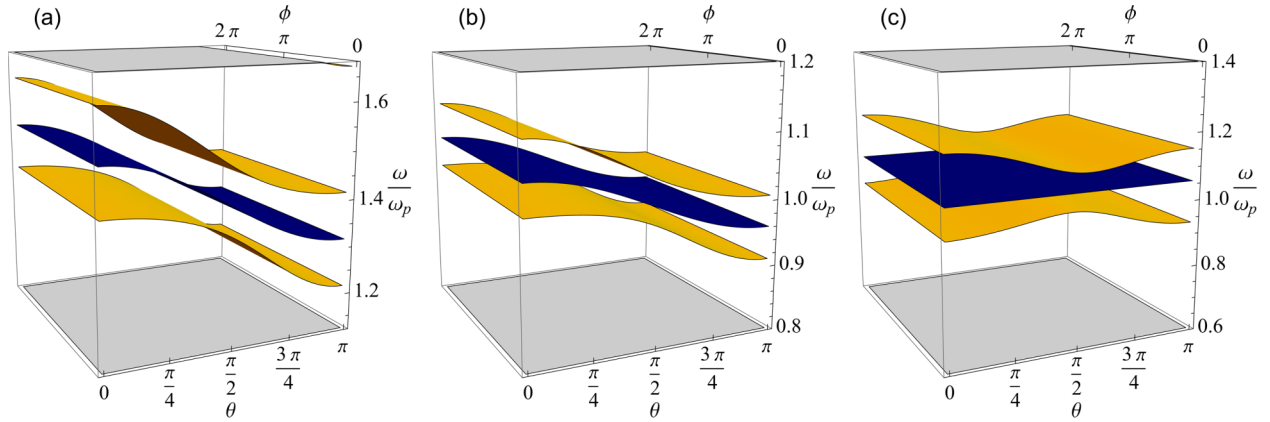


FIG. 8. In yellow: dispersion surfaces of the modes in a 3D momentum sphere surrounding a Weyl point, parametrized by the spherical coordinates θ and ϕ . In blue: real part of complex frequency integral path $\omega_{\text{gap}}(\theta, \phi)$. (a) Local model, at $k_z = +k_z^W$ with $\omega_c = 0.8\omega_p$, $\omega'_p = \sqrt{2}\omega_p$, $A = 0.07$, and $k = k_z^W/5$. (b) Hydrodynamic model, at $k_z = +k_z^W$, with $\beta = 0.2c$, $\omega_c = 0.8\omega_p$, $A = 0.05$, and $k = k_z^W/5$. (c) Full-cutoff model, at $k_z = +k_z^{W,1}$, with $k_{\text{max}} = \omega_p/c$, $\omega_c = 0.8\omega_p$, $\omega'_p = \sqrt{2}\omega_p$, and $k = k_z^{W,1}/5$.

momentum one has -1 ($k_z = +k_z^{W,2}$). The latter results are equal to the ones we would obtain for a local model without the uniaxial plasma response ω'_p , in the condition $\omega_c > \omega_p$ (which generates two Weyl pairs) [25]. These computations are in agreement with the results obtained with Approach I. Additionally, with this this approach, we were able to calculate the Weyl charges for the hydrodynamic case, even without a full band gap in the transverse planes.

IV. CONCLUSIONS

In this work we have introduced a first-principles formalism that enables the characterization of Weyl points in 3D dispersive photonic continua. We introduced two calculation methods to find the Weyl charges by means of the photonic Green's function of the medium [15]. In the first calculation approach, the Weyl charge is found from the calculation of gap Chern numbers in planes transverse to the axis that joins a Weyl pair. Conversely, for the second approach the Weyl charge is obtained through the integration of the flux of the Berry curvature over a small spherical surface centered at the relevant Weyl point. This is in contrast to standard methods based on topological band theory, which require the calculation of the eigenvectors at each value of the wave vector.

We have shown an application of the theory for a 3D magnetized plasma, where the \mathcal{T} -breaking enables the existence of Weyl point pairs. When considering a standard local description of the magnetized plasma, a Weyl point pair emerges at the crossing between a flat plasmonic longitudinal mode and a transverse mode. Furthermore, we have also taken into account the effects of spatial dispersion using the hydrodynamic and full-cutoff models. As might be expected, as the Weyl charge only depends on the Berry curvature over a small region of the momentum space centered at the Weyl point, the Weyl charges associated with the local model are not sensitive to the the spatial dispersion effects in the medium. However, the number and type of Weyl points depend on the nonlocality model, even if the parameter that controls the nonlocal effects is arbitrarily small. As a consequence, knowledge of the topological properties of a 3D system allows us to infer the

gap Chern numbers of the corresponding 2D subsystems (provided they are fully gapped). Our results are hence connected with the gap Chern numbers of the magnetized plasma 2D TM bands, which depend critically on the asymptotic behavior of the material response at $k = \infty$ and thus on the chosen nonlocal model.

Previous literature studied the gap Chern numbers in translationally invariant magnetized plasmas [15,33,35,36], which corresponds to $k_z = 0$ in the plots shown in Fig. 9. Consistent with those studies, in our analysis of the topological properties of the 3D magnetized plasma, we find two relevant band gaps at zero momentum. In the three considered models (local, hydrodynamic, and full-cutoff), the high-frequency band gap (highlighted in blue) is bounded by a Weyl point pair, which gives rise to its topological nature: the gap Chern number is 1 for the local and full-cutoff models, while the hydrodynamic model does not feature a full band gap in the transverse plane. However, the low-frequency band gap (in orange) has an ill-defined topology in the local model, while it is trivial in the hydrodynamic model. Critically, in the full-cutoff model, an outer pair of Weyl points appears which bounds this low-frequency band gap, giving it a nontrivial gap Chern number of -1 . When the cutoff is suppressed $k_{\text{max}} \rightarrow \infty$, the outer Weyl point pair goes to infinity, and the local model with the uniaxial response is retrieved, where only the inner Weyl pair arises. Therefore, our results show how the different topological properties of the 2D system for the different models arise due to the Weyl points present in the 3D bands.

In conclusion, we have presented a detailed study of 3D gapless phases in dispersive photonic continua, and discussed the important effects of nonlocality in the topological properties of these systems. Specifically, we made use of the link between the topological charge of the 3D Berry curvature singularities (Weyl points) and the gap Chern numbers of 2D subsystems, to characterize from first principles the topological properties of an electromagnetic continuum in 3D for the first time. Our results are based on first-principle calculations of topological invariants that naturally take into account frequency dispersion and nonlocality. This methodology can be

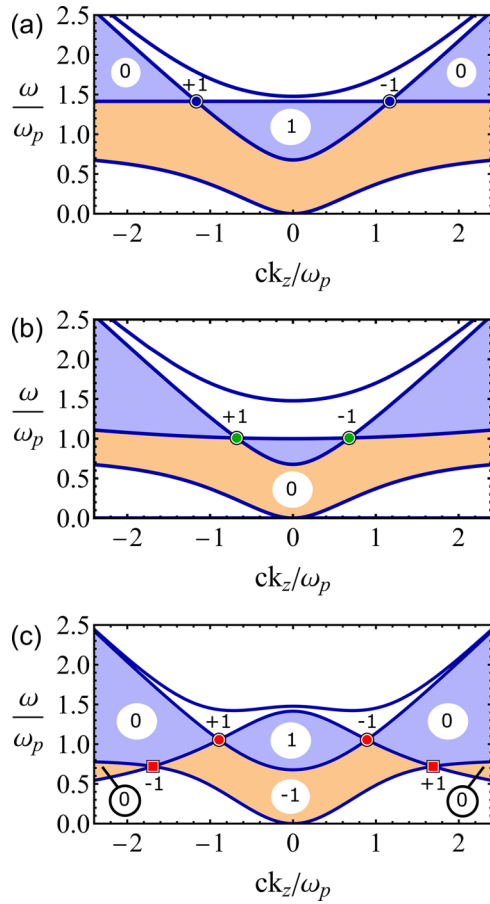


FIG. 9. Summary of the topological characterizations of the local and nonlocal models of the 3D magnetized plasma. The gap Chern numbers in transverse cuts are highlighted with a white circle, for each subregion and they were computed through Approach I [Eqs. (7) and (5)]. The topological charges of the Weyl points, computed through Approach II [Eqs. (1) and (8)] are also showcased. In the three plots we see the k_z axis dispersion for: (a) local model with the Weyl pair as blue circles. Parameters used were $\omega_c = 0.8\omega_p$ and $\omega'_p = \sqrt{2}\omega_p$; (b) hydrodynamic model with the Weyl pair as green circles. The parameters used were $\beta = 0.2c$, $\omega_c = 0.8\omega_p$, and $\omega'_p = \omega_p$; (c) full-cutoff model with the inner Weyl pair as red circles and the outer pair as red squares. The parameters used were $k_{\max} = \omega_p/c$, $\omega_c = 0.8\omega_p$, and $\omega'_p = \sqrt{2}\omega_p$.

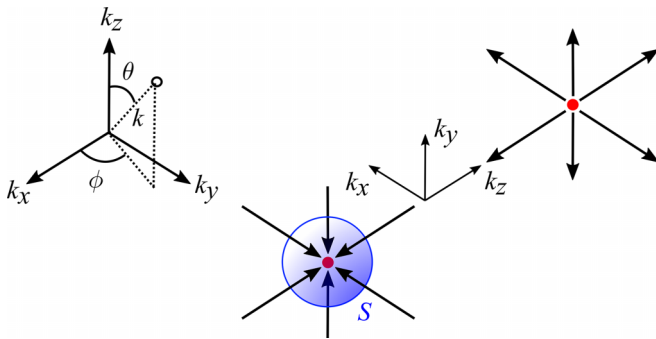


FIG. 10. Geometry and spherical coordinate system adopted for the wave vector space. ϕ is the azimuthal angle, θ is the polar angle and k is the radial distance from the Weyl point, in other terms the radius of the integration sphere, represented in blue.

extended to \mathcal{P} -broken Weyl systems, other 3D topological phases, or to Floquet systems.

ACKNOWLEDGMENTS

We acknowledge funding from Fundação para a Ciência e a Tecnologia and Instituto de Telecomunicações under Projects No. UIDB/50008/2020 and No. 2022.06797.PTDC. P.A.H. acknowledges financial support from the Spanish Ministry of Science and Innovation through the Ramón y Cajal program (Grant No. RYC2021-031568-I), through Project No. PID2022-141036NA-I00 financed by MCIN/AEI/10.13039/501100011033 and FSE+) and from the María de Maeztu Programme for Units of Excellence in R&D (Grant No. CEX2018-000805-M), as well as from the CAM (Grant No. Y2020/TCS-6545). M.G.S. acknowledges support from the Institution of Engineering and Technology (IET) and by the Simons Foundation (Award No. 733700).

APPENDIX A: FREQUENCY-INDEPENDENT DIFFERENTIAL OPERATOR $\hat{L}_{\mathbf{k}}$

Here we show the derivation of the operator \hat{L} from which $\hat{L}_{\mathbf{k}}$ is obtained. We generalize the method of Ref. [37] to the lossless 3D magnetized plasma. We consider the hydrodynamic model as a first instance.

We start with Maxwell's equations in time domain, for propagation in free space ($\partial_t \equiv \frac{\partial}{\partial t}$):

$$-i\nabla \times \mathbf{E} = i\mu_0 \partial_t \mathbf{H}, \quad (\text{A1})$$

$$i(\nabla \times \mathbf{H} - \mathbf{j}) = i\epsilon_0 \partial_t \mathbf{E},$$

where μ_0 and ϵ_0 are the vacuum's permeability and permittivity, respectively. We then consider the continuity equation given by

$$\partial_t \rho + \nabla \cdot \mathbf{j} = 0. \quad (\text{A2})$$

The current \mathbf{j} and charge ρ densities model the response of the dispersive electric gyrotropic material. Making use of Newton's second law of motion plus Lorentz's Force law, the transport equation for a free electron gas biased with a static magnetic field ($\mathbf{B}_0 = B_0 \hat{z}$) is given by

$$\frac{d\mathbf{j}}{dt} = \epsilon_0 \omega_p^2 \mathbf{E} + \frac{q}{m} \mathbf{j} \times \mathbf{B}_0 - \beta^2 \nabla \rho, \quad (\text{A3})$$

where $q = -e$ is the charge of an electron with opposite sign and m is its effective mass. If we wish to retrieve the local model, we just set β as zero. Equations (A1)–(A3) can be rewritten as a Schrödinger-type equation:

$$\hat{L} \cdot \mathbf{Q} = \frac{1}{c} i \partial_t \mathbf{Q}. \quad (\text{A4})$$

The state vector \mathbf{Q} is given by $\mathbf{Q} = [E_x, E_y, E_z, \tilde{H}_x, \tilde{H}_y, \tilde{H}_z, \tilde{j}_x, \tilde{j}_y, \tilde{j}_z, \tilde{\rho}]^T$. We introduce the normalized magnetic field, current and charge density: $\tilde{\mathbf{H}} = \eta_0 \mathbf{H}$, $\tilde{\mathbf{j}} = \eta_0 \mathbf{j}$, $\tilde{\rho} = \eta_0 c \rho$, with η_0 being the vacuum wave impedance and c the speed of light. Since we are interested in the 3D case of the continuous magnetized plasma, we assume a spatial and time variation of the state vector of the type $e^{i\mathbf{k} \cdot \mathbf{r}} e^{-i\omega t}$, with wave vector $\mathbf{k} = k_x \hat{x} + k_y \hat{y} + k_z \hat{z}$. We are also interested in analyzing the dispersion of all light modes

in this medium, and hence the fields and wave vector are unconstrained: $\mathbf{E} = E_x \hat{\mathbf{x}} + E_y \hat{\mathbf{y}} + E_z \hat{\mathbf{z}}$, $\mathbf{H} = H_x \hat{\mathbf{x}} + H_y \hat{\mathbf{y}} + H_z \hat{\mathbf{z}}$ and $\mathbf{j} = j_x \hat{\mathbf{x}} + j_y \hat{\mathbf{y}} + j_z \hat{\mathbf{z}}$ which justifies the dimension of the

state vector written above. By manipulating Eqs. (A1)–(A3), and taking into account that the cyclotron frequency is defined as $\omega_c = -qB_0/m$, we derive the operator \hat{L} :

$$\hat{L}(-i\nabla) = \begin{pmatrix} 0 & 0 & 0 & 0 & -i\partial_z & i\partial_y & -i & 0 & 0 & 0 \\ 0 & 0 & 0 & i\partial_z & 0 & -i\partial_x & 0 & -i & 0 & 0 \\ 0 & 0 & 0 & -i\partial_y & i\partial_x & 0 & 0 & 0 & -i & 0 \\ 0 & i\partial_z & -i\partial_y & 0 & 0 & 0 & 0 & 0 & 0 & 0 \\ -i\partial_z & 0 & i\partial_x & 0 & 0 & 0 & 0 & 0 & 0 & 0 \\ i\partial_y & -i\partial_x & 0 & 0 & 0 & 0 & 0 & 0 & 0 & 0 \\ i\frac{\omega_p^2}{c^2} & 0 & 0 & 0 & 0 & 0 & 0 & -i\frac{\omega_c}{c} & 0 & -i\frac{\beta^2}{c^2}\partial_x \\ 0 & i\frac{\omega_p^2}{c^2} & 0 & 0 & 0 & 0 & i\frac{\omega_c}{c} & 0 & 0 & -i\frac{\beta^2}{c^2}\partial_y \\ 0 & 0 & i\frac{\omega_p^2}{c^2} & 0 & 0 & 0 & 0 & 0 & 0 & -i\frac{\beta^2}{c^2}\partial_z \\ 0 & 0 & 0 & 0 & 0 & 0 & -i\partial_x & -i\partial_y & -i\partial_z & 0 \end{pmatrix}. \quad (\text{A5})$$

The operator $\hat{L}_{\mathbf{k}}$ from Eq. (2) can be obtained by substituting the spatial derivatives in (A5) with the corresponding wave vector components $\frac{\partial}{\partial j} \leftrightarrow ik_j$, $j = \{x, y, z\}$. To get the local model analysed in this work we must set β to zero and include the uniaxial plasma frequency component ω'_p .

The full-cutoff model can be enforced in the system by changing the current density vector \mathbf{j} in Maxwell's equations (A1), replacing it with $(-k_{\max}^{-2} \nabla^2 + 1)^{-1} \mathbf{j}$. The derived operator for this model with the uniaxial plasma frequency ω'_p is given by

$$\hat{L}(-i\nabla) = \begin{pmatrix} 0 & 0 & 0 & 0 & -i\partial_z & i\partial_y & \frac{-i}{(-k_{\max}^{-2} \nabla^2 + 1)} & 0 & 0 & 0 \\ 0 & 0 & 0 & i\partial_z & 0 & -i\partial_x & 0 & \frac{-i}{(-k_{\max}^{-2} \nabla^2 + 1)} & 0 & 0 \\ 0 & 0 & 0 & -i\partial_y & i\partial_x & 0 & 0 & 0 & \frac{-i}{(-k_{\max}^{-2} \nabla^2 + 1)} & 0 \\ 0 & i\partial_z & -i\partial_y & 0 & 0 & 0 & 0 & 0 & 0 & 0 \\ -i\partial_z & 0 & i\partial_x & 0 & 0 & 0 & 0 & 0 & 0 & 0 \\ i\partial_y & -i\partial_x & 0 & 0 & 0 & 0 & 0 & 0 & 0 & 0 \\ i\frac{\omega_p^2}{c^2} & 0 & 0 & 0 & 0 & 0 & 0 & -i\frac{\omega_c}{c} & 0 & 0 \\ 0 & i\frac{\omega_p^2}{c^2} & 0 & 0 & 0 & 0 & i\frac{\omega_c}{c} & 0 & 0 & 0 \\ 0 & 0 & i\frac{\omega_p^2}{c^2} & 0 & 0 & 0 & 0 & 0 & 0 & 0 \\ 0 & 0 & 0 & 0 & 0 & 0 & -i\partial_x & -i\partial_y & -i\partial_z & 0 \end{pmatrix}. \quad (\text{A6})$$

APPENDIX B: NUMERICAL IMPLEMENTATION OF APPROACH II

In this section we describe the direct computation of the Weyl point's topological charge with the first-principles method through Eqs. (1) and (8) (Approach II). Specifically, we will discuss the frequency integral of the equivalent definition of the Berry curvature with the photonic Green's function. Usually, the integral in the complex frequency plane in Eqs. (3), (7), and (8) is taken along a straight line that is parallel to the imaginary frequency axis, centered at a real frequency value ω_{gap} , which is situated in the band gap. This is the case when there exists a well-defined and complete photonic band gap, which separates two distinct eigenmodes [33]. However, with this approach, this is only possible in the case of the full-cutoff model, as discussed in the main text.

For the numerical implementation of this approach, we will adopt the system of spherical coordinates introduced in Sec. II B to parametrize the wave vector space, with polar angle $\theta \in [0, \pi]$, azimuth angle $\phi \in [0, 2\pi[$ and k the radius of the 3D momentum sphere surrounding the

Weyl point. This geometry is highlighted in Fig. 10. The wave vector is thus $\mathbf{k} = \mathbf{k}_W + k\hat{\mathbf{n}}$, where \mathbf{k}_W is the momentum location of the Weyl point and the unit vector normal to the spherical integration surface is parametrized as $\hat{\mathbf{n}} = (\cos \phi \sin \theta, \sin \phi \sin \theta, \cos \theta)$. The charge of a Weyl point can then be computed with the Green's function definition of the Berry curvature (8) through the flux integral

$$\begin{aligned} \mathcal{C}_W &= \frac{1}{2\pi} \int_0^\pi d\theta \int_0^{2\pi} d\phi \mathcal{F}(\mathbf{k}) \cdot \hat{\mathbf{n}} k^2 \sin \theta \\ &= \frac{i}{(2\pi)^2} \int_0^\pi d\theta \int_0^{2\pi} d\phi \int_{\omega_{\text{gap}} - i\infty}^{\omega_{\text{gap}} + i\infty} d\omega \\ &\quad \times g(\omega, \mathbf{k})|_{\mathbf{k}=\mathbf{k}_W + k\hat{\mathbf{n}}} k^2 \sin \theta \\ &= \frac{-1}{(2\pi)^2} \int_0^\pi d\theta \int_0^{2\pi} d\phi \int_{-\infty}^{\infty} d\xi \\ &\quad \times g(\omega, \mathbf{k})|_{\mathbf{k}=\mathbf{k}_W + k\hat{\mathbf{n}}, \omega=\omega_{\text{gap}} + i\xi} k^2 \sin \theta, \end{aligned} \quad (\text{B1})$$

where we performed a coordinate transformation and the integrand function $g(\omega, \mathbf{k})$ can be written

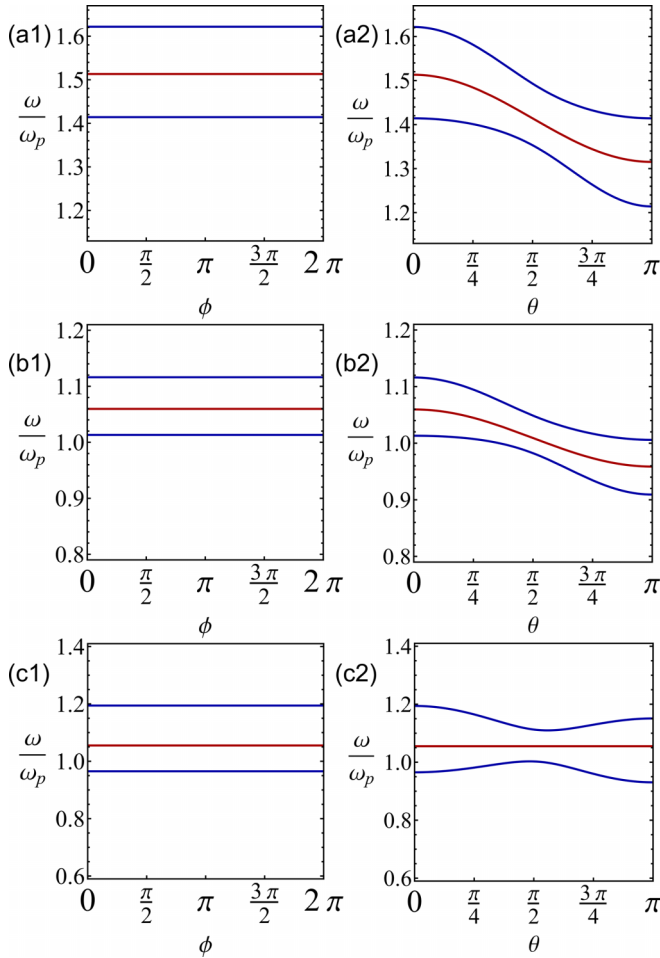


FIG. 11. In blue: frequency dispersion of the modes in a 3D momentum sphere surrounding a Weyl point of the (a) local model at $k_z = +k_z^W$, (b) hydrodynamic model at $k_z = +k_z^W$ and (c) cutoff model at $k_z = +k_z^{W,1}$, parametrized by the spherical coordinates ϕ (a1, b1, c1 with $\theta = 0$) and θ (a2, b2, c2 with $\phi = 0$). In red: real part of complex frequency integral path $\omega_{\text{gap}}(\theta, \phi)$. The parameters used here are the same as in Fig. 8.

explicitly as

$$g(\omega, \mathbf{k}) = \text{Tr} \left\{ [\cos \phi \sin \theta \partial_2 \hat{L}_{\mathbf{k}} \cdot \mathcal{G}_{\mathbf{k}}(\omega) \cdot \partial_3 \hat{L}_{\mathbf{k}} + \sin \phi \sin \theta \partial_3 \hat{L}_{\mathbf{k}} \cdot \mathcal{G}_{\mathbf{k}}(\omega) \cdot \partial_1 \hat{L}_{\mathbf{k}} + \cos \theta \partial_1 \hat{L}_{\mathbf{k}} \cdot \mathcal{G}_{\mathbf{k}}(\omega) \cdot \partial_2 \hat{L}_{\mathbf{k}}] \cdot \mathcal{G}_{\mathbf{k}}^2(\omega) \right\}. \quad (\text{B2})$$

In Fig. 11, we can observe the dispersion plots of the modes in the momentum sphere for the three models, individually in ϕ (with $\theta = 0$) or in θ (with $\phi = 0$). The continuous rotational symmetry of the system about the z axis is clearly manifested in the ϕ plots resulting in a flat frequency dispersion. However, even with a more complex band structure, without this symmetry, it would still be possible to parametrize ω_{gap} , resulting in a more complex surface, and yielding a Weyl charge with this method.

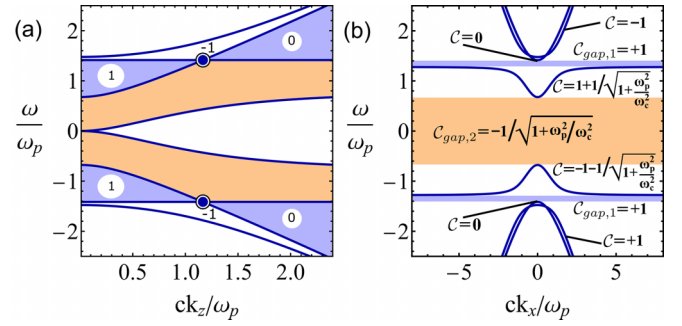


FIG. 12. Frequency dispersion for a local magnetized plasma, featuring negative frequency modes. (a) k_z axis exhibiting the positive momentum Weyl points marked with a blue circle and their topological charge. The band gaps of interest are shaded in blue and orange. The computed gap Chern numbers in transverse cuts are highlighted with a white circle, for each subregion. (b) xoy plane ($k_z = 0$), with Chern numbers for each gap (C_{gap}) and for each band (C) in the insets. The parameters used here were $\omega_c = 0.8\omega_p$ and $\omega'_p = \sqrt{2}\omega_p$.

APPENDIX C: NEGATIVE FREQUENCY MODES

The bands with negative frequency are analyzed in this section. We start by illustrating why the ill-defined topology [33,37,45,47] of the TM mode in the xoy plane of the local magnetized plasma does not affect the topology of the high-frequency band gap, even though the gap Chern number is a sum of the individual Chern numbers of the bands below the band gap. Figure 12(b) shows the gap Chern numbers C_{gap} and the band Chern numbers C in the xoy plane ($k_z = 0$) of the local model. The gap Chern numbers are frequency-symmetric $C_{\text{gap}}(\omega) = C_{\text{gap}}(-\omega)$, while the band Chern numbers of bands linked by the particle-hole symmetry have opposite signs. The latter property explains why the high-frequency band gap (shaded in blue) in the xoy plane of the local model has a well-defined topology, because the noninteger Chern numbers

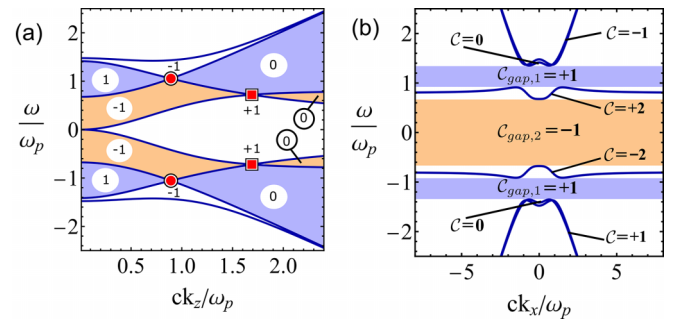


FIG. 13. Frequency dispersion for a full-cutoff model of a magnetized plasma, featuring negative frequency modes. (a) k_z axis exhibiting the positive momentum Weyl points marked with a red circle for the inner ones, with a red square for the outer ones and their topological charge. The band gaps of interest are shaded in blue and orange. The computed gap Chern numbers in transverse cuts are highlighted with a white circle, for each subregion. (b) xoy plane ($k_z = 0$), with Chern numbers for each gap (C_{gap}) and for each band (C) in the insets. The parameters used here were $k_{\text{max}} = \omega_p/c$, $\omega_c = 0.8\omega_p$, and $\omega'_p = \sqrt{2}\omega_p$.

of the low-frequency TM mode and its negative counterpart cancel each other.

A similar analysis of the full frequency spectrum is done for the full-cutoff model in Fig. 13. Since the gap Chern numbers are even-symmetric with respect to frequency, Weyl

points with equal momentum but opposite frequency values have identical topological charge. This property is shown in panel (a) of Figs. 12 and 13. The band Chern numbers are the analytical results from Ref. [33] and they were computed with the theory from Ref. [15].

-
- [1] S. Raghu and F. D. M. Haldane, Analogs of quantum-Hall-effect edge states in photonic crystals, *Phys. Rev. A* **78**, 033834 (2008).
- [2] F. D. M. Haldane and S. Raghu, Possible realization of directional optical waveguides in photonic crystals with broken time-reversal symmetry, *Phys. Rev. Lett.* **100**, 013904 (2008).
- [3] T. Ozawa, H. M. Price, A. Amo, N. Goldman, M. Hafezi, L. Lu, M. C. Rechtsman, D. Schuster, J. Simon, O. Zilberberg, and I. Carusotto, Topological photonics, *Rev. Mod. Phys.* **91**, 015006 (2019).
- [4] M. S. Rider, S. J. Palmer, S. R. Pockock, X. Xiao, P. A. Huidobro, and V. Giannini, A perspective on topological nanophotonics: Current status and future challenges, *J. Appl. Phys.* **125**, 120901 (2019).
- [5] L. Lu, J. D. Joannopoulos, and M. Soljai, Topological photonics, *Nat. Photon.* **8**, 821 (2014).
- [6] M. Kim, Z. Jacob, and J. Rho, Recent advances in 2D, 3D and higher-order topological photonics, *Light Sci. Appl.* **9**, 130 (2020).
- [7] M. G. Silveirinha, Bulk-edge correspondence for topological photonic continua, *Phys. Rev. B* **94**, 205105 (2016).
- [8] M. G. Silveirinha, Proof of the bulk-edge correspondence through a link between topological photonics and fluctuation-electrodynamics, *Phys. Rev. X* **9**, 011037 (2019).
- [9] Z. Wang, Y. Chong, J. D. Joannopoulos, and M. Soljai, Observation of unidirectional backscattering-immune topological electromagnetic states, *Nature (London)* **461** (2009).
- [10] Y. Hatsugai, Chern number and edge states in the integer quantum Hall effect, *Phys. Rev. Lett.* **71**, 3697 (1993).
- [11] A. M. Essin and V. Gurarie, Bulk-boundary correspondence of topological insulators from their respective Green's functions, *Phys. Rev. B* **84**, 125132 (2011).
- [12] C. L. Kane and E. J. Mele, Z_2 topological order and the quantum spin Hall effect, *Phys. Rev. Lett.* **95**, 146802 (2005).
- [13] M. C. Rechtsman, J. M. Zeuner, Y. Plotnik, Y. Lumer, D. Podolsky, F. Dreisow, S. Nolte, M. Segev, and A. Szameit, Photonic floquet topological insulators, *Nature (London)* **496**, 196 (2013).
- [14] A. B. Khanikaev, S. Hossein Mousavi, W.-K. Tse, M. Kargarian, A. H. MacDonald, and G. Shvets, Photonic topological insulators, *Nat. Mater.* **12**, 233 (2013).
- [15] M. G. Silveirinha, Chern invariants for continuous media, *Phys. Rev. B* **92**, 125153 (2015).
- [16] M. G. Silveirinha, z_2 topological index for continuous photonic materials, *Phys. Rev. B* **93**, 075110 (2016).
- [17] D. E. Fernandes and M. G. Silveirinha, Topological origin of electromagnetic energy sinks, *Phys. Rev. Appl.* **12**, 014021 (2019).
- [18] D. E. Fernandes, R. A. M. Pereira, S. Lannebère, T. A. N. Morgado, and M. G. Silveirinha, Experimental verification of ill-defined topologies and energy sinks in electromagnetic continua, *Adv. Photon.* **4**, 035003 (2022).
- [19] H. Qin and Y. Fu, Topological Langmuir-cyclotron wave, *Sci. Adv.* **9**, eadd8041 (2023).
- [20] L. Lu, L. Fu, J. D. Joannopoulos, and M. Soljai, Weyl points and line nodes in gyroid photonic crystals, *Nat. Photon.* **7**, 294 (2013).
- [21] S. Howard, L. Jiao, Z. Wang, N. Morali, R. Batabyal, P. Kumarnag, N. Avraham, H. Beidenkopf, P. Vir, E. Liu, C. Shekhar, C. Felser, T. Hughes, and V. Madhavan, Evidence for one-dimensional chiral edge states in a magnetic Weyl semimetal $\text{Co}_3\text{Sn}_2\text{S}_2$, *Nat. Commun.* **12**, 4269 (2021).
- [22] M. Xiao, Q. Lin, and S. Fan, Hyperbolic Weyl point in reciprocal chiral metamaterials, *Phys. Rev. Lett.* **117**, 057401 (2016).
- [23] B. Yang, Q. Guo, B. Tremain, L. E. Barr, W. Gao, H. Liu, B. Béri, Y. Xiang, D. Fan, A. P. Hibbins, and S. Zhang, Direct observation of topological surface-state arcs in photonic metamaterials, *Nat. Commun.* **8**, 97 (2017).
- [24] Y. Yang, W. Gao, L. Xia, H. Cheng, H. Jia, Y. Xiang, and S. Zhang, Spontaneous emission and resonant scattering in transition from type I to type II photonic Weyl systems, *Phys. Rev. Lett.* **123**, 033901 (2019).
- [25] W. Gao, B. Yang, M. Lawrence, F. Fang, B. Béri, and S. Zhang, Photonic Weyl degeneracies in magnetized plasma, *Nat. Commun.* **7**, 12435 (2016).
- [26] F. Yichen and Q. Hong, Topological phases and bulk-edge correspondence of magnetized cold plasmas, *Nat. Commun.* **12** (2021).
- [27] L. Lu, Z. Wang, D. Ye, L. Ran, L. Fu, J. D. Joannopoulos, and M. Soljai, Experimental observation of Weyl points, *Science* **349**, 622 (2015).
- [28] S. Vaidya, J. Noh, A. Cerjan, C. Jörg, G. von Freymann, and M. C. Rechtsman, Observation of a charge-2 photonic Weyl point in the infrared, *Phys. Rev. Lett.* **125**, 253902 (2020).
- [29] D. Wang, B. Yang, W. Gao, H. Jia, Q. Yang, X. Chen, M. Wei, C. Liu, M. Navarro-Cía, J. Han, W. Zhang, and S. Zhang, Photonic Weyl points due to broken time-reversal symmetry in magnetized semiconductor, *Nat. Phys.* **15**, 1150 (2019).
- [30] M. Kim, W. Gao, D. Lee, T. Ha, T.-T. Kim, S. Zhang, and J. Rho, Extremely broadband topological surface states in a photonic topological metamaterial, *Adv. Opt. Mater.* **7**, 1900900 (2019).
- [31] M. Blanco de Paz, C. Devescovi, G. Giedke, J. J. Saenz, M. G. Vergniory, B. Bradlyn, D. Bercioux, and A. García-Etxarri, Tutorial: Computing topological invariants in 2D photonic crystals, *Adv. Quantum Technol.* **3**, 1900117 (2020).
- [32] D. Vanderbilt, *Berry Phases in Electronic Structure Theory: Electric Polarization, Orbital Magnetization and Topological Insulators* (Cambridge University Press, Cambridge, UK, 2018).

- [33] M. G. Silveirinha, Topological classification of Chern-type insulators by means of the photonic Green function, *Phys. Rev. B* **97**, 115146 (2018).
- [34] S. A. Hassani Gangaraj, A. Nemilentsau, and G. W. Hanson, The effects of three-dimensional defects on one-way surface plasmon propagation for photonic topological insulators comprised of continuum media, *Sci. Rep.* **6**, 30055 (2016).
- [35] S. A. Hassani Gangaraj and F. Monticone, Physical violations of the bulk-edge correspondence in topological electromagnetics, *Phys. Rev. Lett.* **124**, 153901 (2020).
- [36] S. Pakniyat, S. A. H. Gangaraj, and G. W. Hanson, Chern invariants of topological continua: A self-consistent nonlocal hydrodynamic model, *Phys. Rev. B* **105**, 035310 (2022).
- [37] F. R. Prudêncio and M. G. Silveirinha, Ill-defined topological phases in local dispersive photonic crystals, *Phys. Rev. Lett.* **129**, 133903 (2022).
- [38] R. Bianco and R. Resta, Mapping topological order in coordinate space, *Phys. Rev. B* **84**, 241106(R) (2011).
- [39] S. A. R. Horsley, Topology and the optical Dirac equation, *Phys. Rev. A* **98**, 043837 (2018).
- [40] T. Misawa and Y. Yamaji, Zeros of Green functions in topological insulators, *Phys. Rev. Res.* **4**, 023177 (2022).
- [41] A. Cerjan and T. A. Loring, An operator-based approach to topological photonics, *Nanophotonics* **11**, 4765 (2022).
- [42] N. P. Armitage, E. J. Mele, and A. Vishwanath, Weyl and Dirac semimetals in three-dimensional solids, *Rev. Mod. Phys.* **90**, 015001 (2018).
- [43] H. Nielsen and M. Ninomiya, The Adler-Bell-Jackiw anomaly and Weyl fermions in a crystal, *Phys. Lett. B* **130**, 389 (1983).
- [44] M. G. Silveirinha, Topological theory of non-Hermitian photonic systems, *Phys. Rev. B* **99**, 125155 (2019).
- [45] F. R. Prudêncio and M. G. Silveirinha, First principles calculation of the topological phases of the photonic Haldane model, *Symmetry* **13**, 2229 (2021).
- [46] J. a. C. Serra and M. G. Silveirinha, Rotating spacetime modulation: Topological phases and spacetime Haldane model, *Phys. Rev. B* **107**, 035133 (2023).
- [47] F. R. Prudêncio and M. G. Silveirinha, First principles calculation of topological invariants of non-Hermitian photonic crystals, *Commun. Phys.* **3**, 221 (2020).
- [48] U. K. Chettiar, A. R. Davoyan, and N. Engheta, Hotspots from nonreciprocal surface waves, *Opt. Lett.* **39**, 1760 (2014).
- [49] J. A. Kong, *Electromagnetic Wave Theory*, 7th ed. (EMW Publishing, New York, USA, 2008).
- [50] E. D. Palik, R. Kaplan, R. W. Gammon, H. Kaplan, R. F. Wallis, and J. J. Quinn, Coupled surface magnetoplasmon-optic-phonon polariton modes on InSb, *Phys. Rev. B* **13**, 2497 (1976).
- [51] M. G. Silveirinha, Topological angular momentum and radiative heat transport in closed orbits, *Phys. Rev. B* **95**, 115103 (2017).
- [52] F. D. M. Haldane, Berry curvature on the Fermi surface: Anomalous Hall effect as a topological Fermi-liquid property, *Phys. Rev. Lett.* **93**, 206602 (2004).
- [53] L. D. Landau, J. S. Bell, M. Kearsley, L. Pitaevskii, E. Lifshitz, and J. Sykes, *Electrodynamics of Continuous Media* (Elsevier, Amsterdam, 2013), Vol. 8.
- [54] J. A. Bittencourt, *Fundamentals of Plasma Physics* (Springer, Berlin, 2004).